J Mol Model (2011) 17:1707–1717
DOI 10.1007/s00894-010-0866-6

ORIGINAL PAPER

The application of inverse Broyden's algorithm for modeling of crack growth in iron crystals

Igor Telichev · Oleg Vinogradov

Received: 6 June 2010 / Accepted: 29 September 2010 / Published online: 2 November 2010

Abstract In the present paper we demonstrate the use of inverse Broyden's algorithm (IBA) in the simulation of fracture in single iron crystals. The iron crystal structure is treated as a truss system, while the forces between the atoms situated at the nodes are defined by modified Morse inter-atomic potentials. The evolution of lattice structure is interpreted as a sequence of equilibrium states corresponding to the history of applied load/deformation, where each equilibrium state is found using an iterative procedure based on IBA. The results presented demonstrate the success of applying the IBA technique for modeling the mechanisms of elastic, plastic and fracture behavior of single iron crystals.

Keywords Atomistic simulation · Molecular statics · Inverse Broyden's algorithm · Crack growth

Introduction

Crack tip dislocation emission constitutes the re-arrangement of atomic positions and atomic bonds in a crystal structure near a crack tip. These dislocations are the precursors of crack growth and their study is the first step in understanding the evolution of material degradation. The present paper concerns the use of Inverse Broyden's Algorithm (IBA) as a simulation tool for fracture phenomena in iron crystals. In earlier work [1], we showed that the IBA can handle problems of high non-linearity, including the positive-to-negative transition of element stiffness. In order to demonstrate the potential of IBA to study the processes of nano-scale deformation and fracture, this technique is used in the present paper to simulate atomic-scale crack growth in two-dimensional (2D) and three-dimensional (3D) iron structures.

I. Telichev (✉)
Department of Mechanical and Manufacturing Engineering,
University of Manitoba,
75A Chancellors Circle, E2-327 Engineering Bldg.,
Winnipeg, Manitoba R3T 5V6, Canada
e-mail: telichev@cc.umanitoba.ca

O. Vinogradov
Department of Mechanical and Manufacturing Engineering,
University of Calgary,
2500 University Drive NW,
Calgary, AB T2N 1N4, Canada

Methods

The present approach falls into the Molecular Statics (MS) formulation framework, where the iron crystal structure is treated as a truss system, the forces between the atoms situated at the nodes are defined by the inter-atomic potential, and the evolution of lattice structure is considered as a sequence of constrained equilibrium states.

The time-independent MS approach is used widely in problems dealing with crack formation and growth [2–7]. A limitation of this approach is that the simulation is performed for a 0°K temperature, but it has the advantage that it allows the dynamic process of cracking to be followed in a quasi-static manner, which in molecular dynamics would be possible only by extraordinarily long time trajectories.

As demonstrated in earlier work [1], the equilibrium state of the atomic structure at each loading step can be described by the following non-linear algebraic system of equations: $[\mathbf{K}]\{\mathbf{D}\}=\{\mathbf{R}\}_A$, where $[\mathbf{K}]$ is the global stiffness matrix, which is a function of displacements and thus varies at each iterative step; $\{\mathbf{D}\}$ is the nodal displacement vector; and $\{\mathbf{R}\}_A$ is the external load vector.

The IBA represents the generalization of the Secant method extended to systems of nonlinear equations. The important feature of the IBA method is that it deals with updating the inverse of the global stiffness matrix and not with the stiffness matrix itself. The computation involves only matrix multiplication at each step and as such requires $\boldsymbol{O}(N^2)$ arithmetic calculations, which constitutes a considerable improvement compared with Newton's method, where $\boldsymbol{O}(N^3)$ arithmetic operations are necessary to solve the system [8]. To start the procedure we need an initial approximation $[\mathbf{K}]_0$ and its inverse $[\mathbf{Z}]_0$. Then, at each iteration, $[\mathbf{Z}]_0$ is improved by the addition of a matrix update, expressed by the second term in the following equation.

$$[\mathbf{Z}]_i = [\mathbf{Z}]_{i-1} + \frac{\left(\{\Delta\mathbf{D}\}_i - [\mathbf{Z}]_{i-1}\{\mathbf{y}\}_i\right)\{\Delta\mathbf{D}\}_i^T[\mathbf{Z}]_{i-1}}{\{\Delta\mathbf{D}\}_i^T[\mathbf{Z}]_{i-1}\{\mathbf{y}\}_i} \tag{1}$$

where i is the iteration number; $\{\Delta\mathbf{D}\}_i=\{\mathbf{D}\}_i - \{\mathbf{D}\}_{i-1}$ is the displacement increment; $\{\Delta\mathbf{R}\}_{i-1}=\{\mathbf{R}\}_A - \{\mathbf{R}\}_{i-1}$ is the load imbalance and $\{\mathbf{y}\}_i=\{\Delta\mathbf{R}\}_i - \{\Delta\mathbf{R}\}_{i-1}$ [9].

The adapted termination criterion for an iterative process was that recommended in [10]:

$$\mathbf{max}(\mathrm{CNORM}, \mathrm{RNORM}) \le 10^{-5} \tag{2}$$

where

$$\mathrm{CNORM} = \left(\sum \Delta D_j^2\right)^{1/2}\left(\sum D_j^2\right)^{-1/2} \tag{3a}$$

$$\mathrm{RNORM} = \left(\sum \Delta R_j^2\right)^{1/2}\left(\sum R_j^2\right)^{-1/2} \tag{3b}$$

ΔD_j, D_j, ΔR_{i-1}, and R_{i-1} denote, respectively, the displacement increment, increment, load increment, and load; CNORM and RNORM are the ratios of Euclidean norms. Further details of the simulation technique are presented in earlier work [1].

Results and discussion

2D computational cell

The specimen shown in Fig. 1 represents the main 2D simulation cell in this work: the solid has been discretized as a triangular lattice, which is equivalent to the (0001) plane in a hexagonal crystal. The finite-length nano-crack was produced at the center of lattice by removing eight atoms from the central row. Each node of a 2D network was connected by bonds to the six nearest neighbors, and to the six second neighbors, as depicted in Fig. 2.

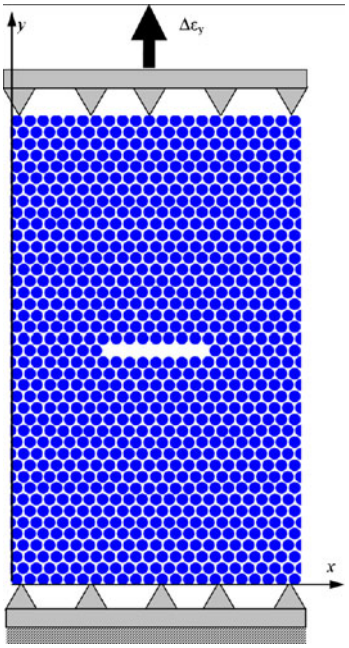

Fig. 1 Set-up for two-dimensional (2D) numerical experiments

The modified Morse potential developed by Fujiwara and Ishii [11] was used to describe the iron–iron interatomic interactions. According to the Morse function, the potential energy of two atoms separated by the distance r is defined as following:

$$\phi_{\mathrm{Morse}}(\mathrm{x}) = \varepsilon_{Morse}\left(\mathrm{e}^{-2\mathrm{m}(\mathrm{x}-1)} - 2\mathrm{e}^{-\mathrm{m}(\mathrm{x}-1)}\right) \tag{4}$$

where $x=r/r_e$ is interatomic distance (dimensionless); r is interatomic distance (Å); r_e is equilibrium distance (Å); $\varepsilon_{\mathrm{Morse}}$ and m are constants. The following Morse potential parameters were used: a=2.867 [Å]; r_e=0.993a [Å]; m=3.95; $\varepsilon_{\mathrm{Morse}}$=9.63 kcal mol^{-1} [11, 12]; in the modified Morse potential of Fe–Fe, the long-range tail of the original

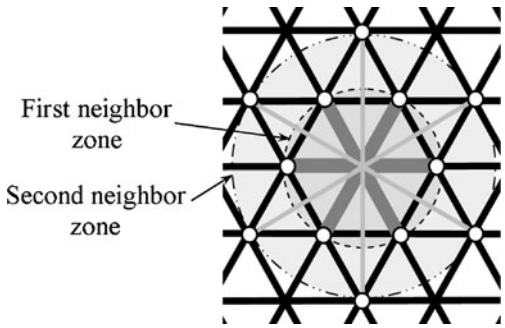

Fig. 2 2D triangular lattice and first- and second-neighbors

Morse potential was truncated by using a function $f(x)$. So the modified Morse potential takes the form:

$$\phi_{\text{Modified}}(x) = \phi_{\text{Morse}}(x) \times f(x), \tag{5}$$

where

$$f(x) = \begin{cases} 1 & x < 1 \\ 3z^4 - 8z^3 + 6z^2 & x_c > x > 1 \\ 0 & x > x_c \end{cases} \tag{6}$$

$$z = (x - x_c)/(1 - x_c);\ x_c = r_{cut-off}/r_e = 1.4[11].$$

2D tensile test

The simulations were performed on lattices consisting of 41 horizontal atomic rows lying one upon the other. Each odd row contained 40 atoms and each even row 41 atoms, respectively, thus the whole lattice had 1,660 atoms in total. The lower row of atoms was held fixed while the top boundary atoms were displaced upward.

The evolution of the atomic configuration is shown in Fig. 3, where each frame corresponds to a particular strain

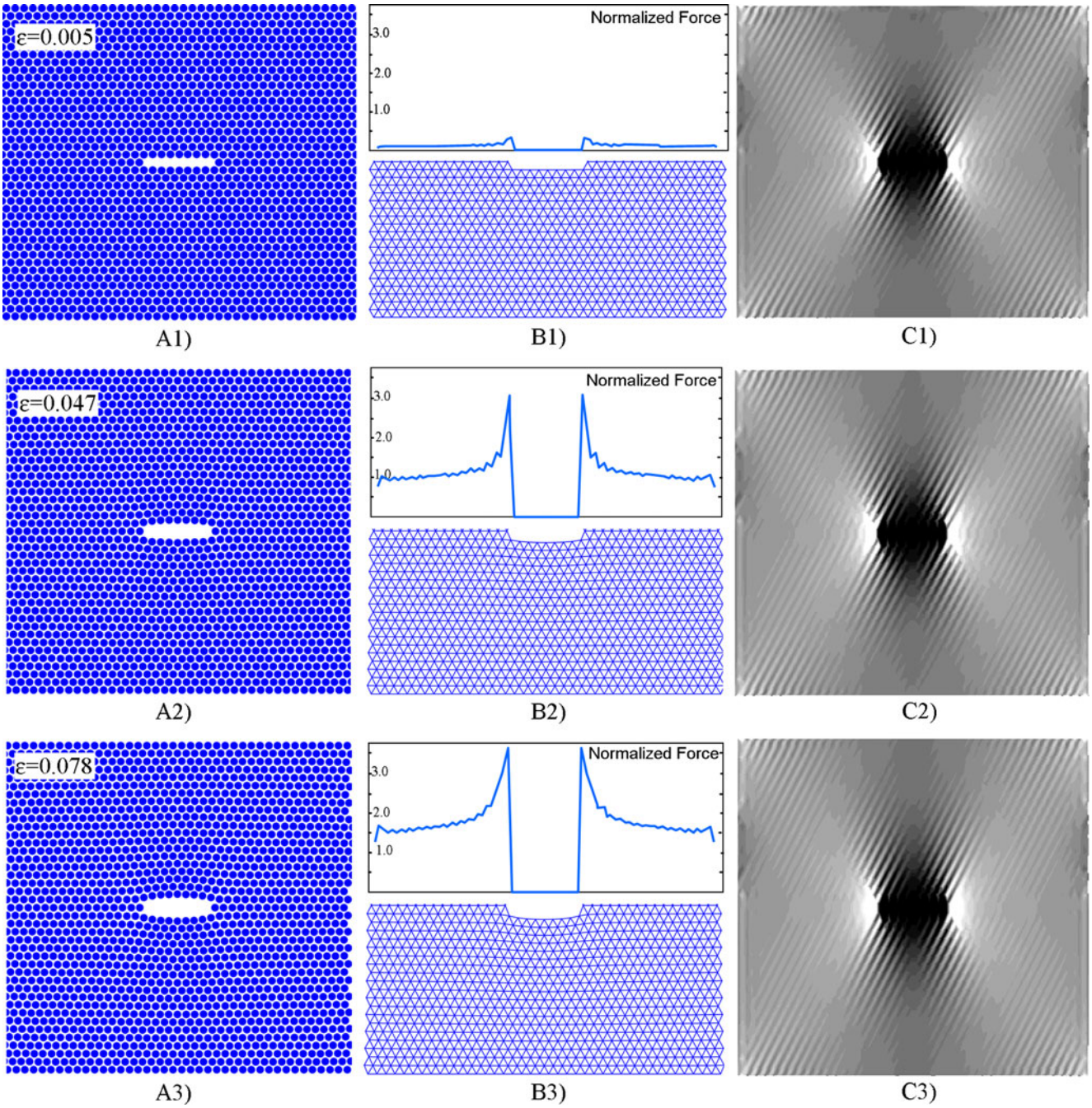

Fig. 3a–c Accumulation of defects and evolution of force field. **a** Structure, **b** atomic force network, **c** force field pattern

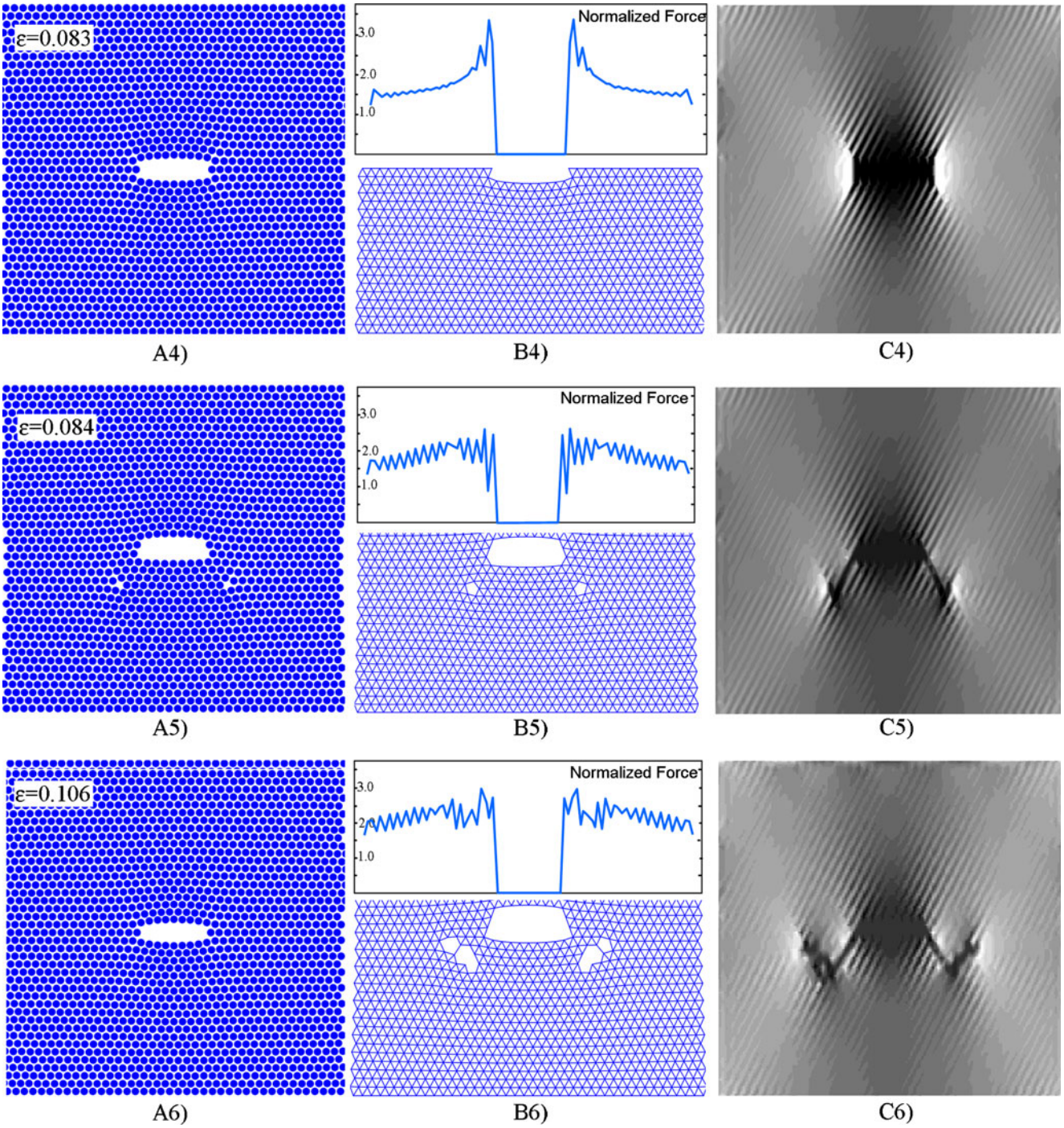

Fig. 3 (continued)

level ranging from 0.005 to 0.106. In this figure, the first column of frames, denoted as A1–A6, shows the positions of atoms during the simulation run. The second column (B1–B6) illustrates the evolution of the atomic bonds network (for a better visual representation only the first-neighbor bonds are shown). It also shows the curve of force distribution in the vicinity of the crack tip.

Frames C1–C6 from the last column illustrate the force field pattern within the whole structure and its change under the loading. As shown, when the load increases, zones of high and low tensile force are formed. The white color in Fig. 3c denotes the highest force and black the lowest. One can see that "shadow" zones of low tensile force have appeared under and above the crack, while zones of high

tensile force have formed near the crack tip (Fig. 3, frames C1–C4). With the increase of applied strain, the intensity of force in the vicinity of crack tips also increases. This trend holds at ε=0.083, when the tensile force near the crack tips reaches its maximum (Fig. 3; B4, C4). At this strain the symmetrical inclined slip lines emanating from the crack tips are formed as seen in Figs. 3(A4) and 4a.

With increasing strain (ε=0.084), emission of edge dislocations from the crack tip occurs; two edge dislocations are emitted on slip planes formed earlier, blunting the crack tip. Figures 3 (A5, B5, C5) and 4b show the relaxed structure after the emission of first two dislocations, illustrating that the appearance of dislocations decreases the force intensity near the crack tips and causes the

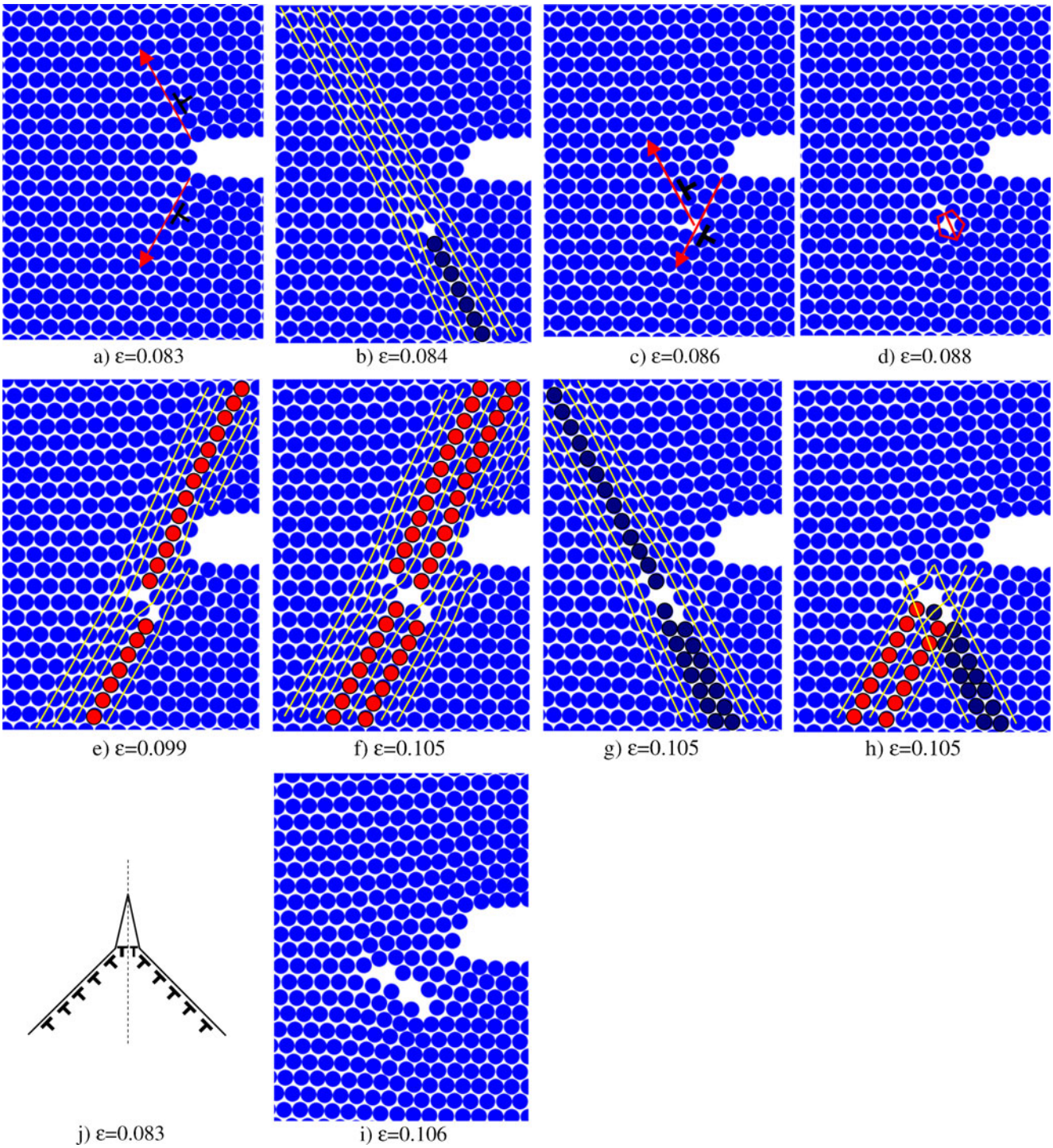

Fig. 4 Stages of defect accumulation

formation of two point defects at the points of slip line and dislocation intersection. Further loading results in the sliding of atoms along the new slip line, as is clearly discernible in frame A5 (Fig. 3).

The former and new slip lines are indicated in Fig. 4c by red arrows. Figure 4 shows the damage accumulation patterns in the crack tip region in detail. The process of slipping of atomic planes leads to the formation of a small twinned region (Fig. 4d), and generation and accumulation of edge dislocation arrays along the new slip plane (Figs. 4e, f). The coalescence of glide dislocations on intersecting slip planes opens up a new microcrack (Fig. 4h, i). This represents crack nucleation via the mechanism proposed by Cottrell [13] (Fig. 4j). The evolution of force field patterns in the process of micro-crack nucleation is shown in frames C5, C6 (Fig. 3). These frames demonstrate that crack nucleation causes the release of force intensity near the tips of the initial crack, and transmission of highest force concentration to the area adjacent to the tips of newly nucleated microcracks.

3D computational cell

The specimen shown in Fig. 5 represents a 3D simulation cell in this work, where x, y, z are global coordinates. A periodic boundary condition is imposed along the z-direction to simulate plane strain conditions (Fig. 6). A single crystal was composed by {001} planes and the crack plane (010) was chosen from the analysis performed in [3] to facilitate easier brittle cleavage, so that the most dangerous case would be considered.

The central finite-length nano-crack was obtained by removing a monolayer of iron atoms so that the crack ultimately had a sharp tip. A single crystal with a crack of eight lattice parameters in length was considered as a reference structure for further simulations. Thus a classical scheme was considered: a plate of finite width $2W$ with a central crack length $2l$.

In terms of lattice parameter (a), the interatomic distances between the reference atom and its first, second and third nearest neighbors, respectively, can be expressed as follows: $r_1=(\sqrt{3}/2)a$, $r_2=a$, $r_3=(\sqrt{2})a$, where $a=r_e/0.993$. Since the Fujiwara-Ishii potential converges smoothly to zero at the distance $r_{\text{cut-off}}/r_e=1.4$, it means that the interactions of other than first- and second-nearest neighbor can be ignored.

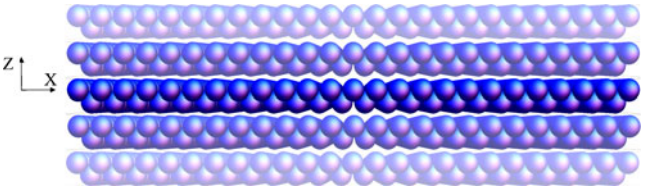

Fig. 6 Scheme of periodic boundary imposed along the z-direction

The first and second nearest neighbors of the reference iron atom are shown in Fig. 7. Two grey vectors r_2^{out} highlight the out-of-plane second nearest neighbors, i.e., second nearest neighbors of the reference atom that belong to different {001} planes. Figure 7 illustrates the fact that, due to the symmetry imposed by the periodic boundary condition in the z-direction, the out-of-plane second-nearest neighbors produce inter-atomic forces that are equal in magnitude and opposite in direction. Besides, these forces are negligibly small since the interatomic distances in this case $\left(r_2^{out}\right)$ are equal to the lattice parameter $a=r_e/0.993$ and they are not going to change in the y-direction during the tensile test because of the periodic boundary condition. Thus, the effect of out-of-plane second-nearest neighbors can be ignored and only first nearest neighbors and in-plane second nearest neighbors need be considered in the simulation.

To represent the body-centred cubic (bcc) iron structure we used the periodical scheme that was previously applied in simulations [3, 14]. The simulation cell contained two atomic layers in thickness along the direction of plane strain (z-direction) and, as mentioned above, the simulation cell was periodic in this direction (Fig. 6).

In order to simulate uniaxial tensile loading in the y-direction, the lower plane of the sample was fixed while constant displacement increments were applied to all atoms

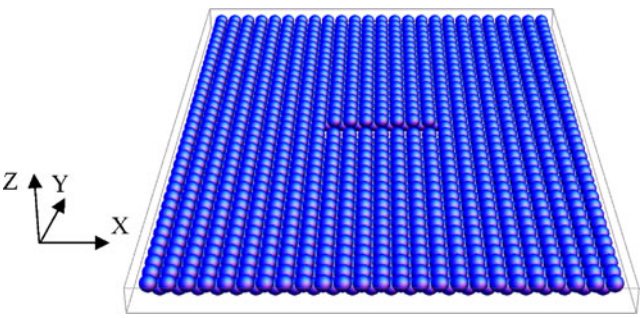

Fig. 5 Three-dimensional (3D) computational cell with embedded nano-crack

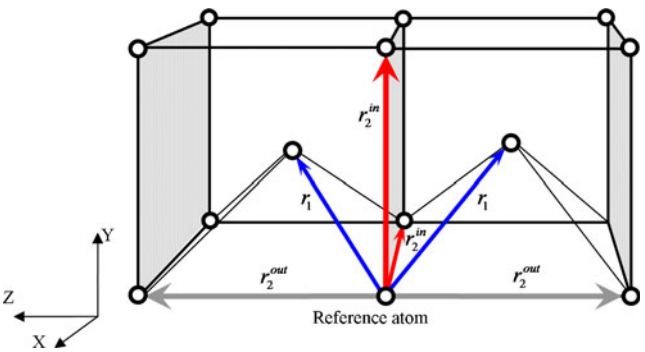

Fig. 7 First and second nearest neighbors in body-centred cubic (bcc) iron structure

Table 1 Modulus of elasticity and the critical stress obtained for different *l/W*-ratios

l/W	0.50	0.40	0.33	0.29	0.27	0.25
σ_c, GPa	11.4	11.9	12.6	12.5	12.6	12.7
E, GPa	163.8	193.6	215.3	210.1	214.5	216.3

in the upper plane. The vertical boundaries were considered to be free surfaces.

Formal analysis included the search of equilibrium configurations for the 3D discrete structure. Before the first loading, the structure was relaxed to an equilibrium state using the IBA [9]. Similarly, the structure was relaxed after each incremental displacement.

To insure that free boundaries do not affect the computational results in the nano-scale tests the calculations were carried out for different *l/W*-ratios of the structure.

To explore the *l/W*-ratio effect, stress-strain curves were obtained for *l/W*-ratios ranging from 0.25 to 0.50. The variation of *l/W*-ratio was achieved by altering the ligament—the distance between the crack tip and the lateral edge of the structure, while the crack length was kept constant.

In terms of a lattice parameter, the structure width, as well as the crack length, is described by the integer number. Thus, the *l/W*-ratio changed in a discrete manner and its range of 0.25–0.50 corresponded to a range of the ligament varied from 4 to 12 lattice parameters.

Two characteristics of the stress-strain curves—the modulus of elasticity and the critical stress—were selected for the analysis. The results of σ_c and *E* calculation for the various *l/W*-ratios are presented in Table 1 and Fig. 8.

Figure 8 illustrates that a structure with *l/W*=0.33 is large enough to avoid any significant effects of free boundaries while preserving the basic properties of the system. Based on this observation, the sample with *l/W*=0.33 was considered as a reference structure. For a chosen crack of length 8 lattice parameters, the ratio *l/W*=0.33 corresponds to a crystal of 24 lattice parameters wide with a ligament 8 lattice parameters long.

For all computational experiments, we used specimens with a height (*2H*) of 38 lattice parameters, which corresponded to *H/W*=1.58 for chosen *l* and *W*. We did not change the vertical geometrical dimension of the specimen to study the effect of *H/W*-ratio on the computational results. Based on boundary correction factors data for the finite width plate [15], we assumed that, for *H/W*>1.5, the effect of *H/W*-ratio variation is minor.

3D tensile test

Figure 9(A1) illustrates the frontal view (along the [001] direction) of the structure. This is a 2D projection of a 3D computation cell in a (001) plane and it shows two atomic layers. Atoms that belong to the front layer are indicated in blue, while black atoms are located in the next layer behind. The total number of atoms in a computational cell was 1,766. A schematic diagram of such a system is shown in Fig. 9(B1).

In the context of a quasi-static approach, the fracture simulation is interpreted as a series of equilibrium states corresponding to the history of external load/deformation applied to the structure. Figure 10 represents the stress–strain curve obtained in the numerical tensile test. The basic stages of sample degradation are shown in Figs. 9(A1–A9) where each frame corresponds to a particular strain level ranging from 0 to 0.088.

Simulation allows the strain and load to be calculated at every element of atomic structure. This is analogous to having virtual strain gauges at the desired locations within the specimen. Figure 11 illustrates the location of the virtual strain gauges that provide monitoring of the elements lying in the (001) plane. The results of calculation can be viewed as contour plots.

Figure 9(B1–B6) illustrates the evolution of the interatomic force field within the (001) plane under the loading (strain range ε=0–0.070). The white and black colors denote the highest and the lowest levels, respectively, of interatomic force intensity. The first three frames in Fig. 9 represent the pre-critical stage of structure deformation. In pictures B2 and B3, we can observe zones of low tensile

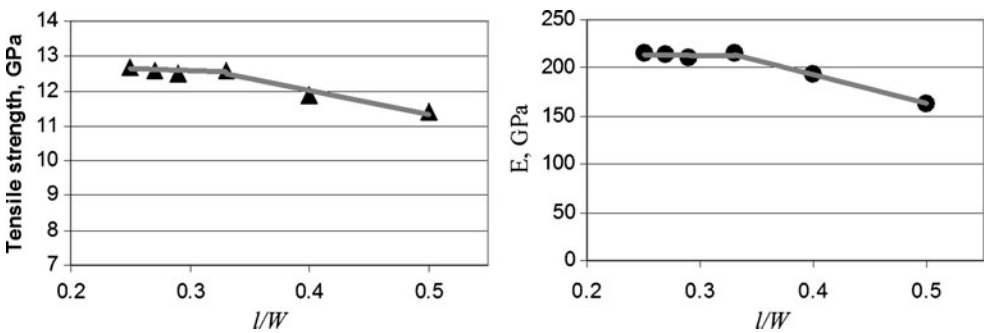

Fig. 8 Variation of the stress-strain curve characteristics

force under and above the crack, and zones of high tensile force formed near the crack tip. For the elastic stage of sample deformation, we can conclude that the higher applied load is the higher force intensity in the vicinity of crack tips.

Picture B3 corresponds to $\varepsilon=0.058$, when the tensile stress reaches its maximum on strain-stress curve (Fig. 10), which is the last point of elastic response of the structure. This maximum (12.6 GPa) was considered as a critical stress (σ_c). It is of interest to compare the obtained numerical result at this point with the available estimates of theoretical tensile strength made for bcc iron. Clatterbuck et al. [16] reported this value amounting to 14.2 GPa. In this respect our result $\sigma_c=12.6$ GPa obtained for the crystal with central atomic-scale crack looks quite reasonable. The obtained critical stress can be also compared with results of the Griffith analysis presented in [3], where bcc iron was modeled using the Finnis-Sinclair and Johnson potentials. Griffith predictions [3] recalculated for the chosen crack length (8 lattice parameters) give $\sigma_c=11.3$ GPa and $\sigma_c=15.5$ GPa for the Finnis-Sinclair and Johnson potentials, respectively, which also constitutes a reasonable agreement with the result presented in this paper (12.6 GPa).

Once the simulation reaches this critical stage, a competition develops between the two possible modes of material response: dislocation nucleation or structure cleavage. Often both of these processes occur simultaneously. The advantage of the truss-type model is that it does not require a priori information about the failure path.

Frame A4 (Fig. 10) illustrates the first stress drop of the sample due to the cleavage-mode of fracture. Crack tip deformation plays a key role in the fracture process: a zone of weakened atomic bonds forms ahead of the crack tip (Fig. 9, B4) and, as the strain applied is increased, this zone keeps propagating toward the free boundary of the sample.

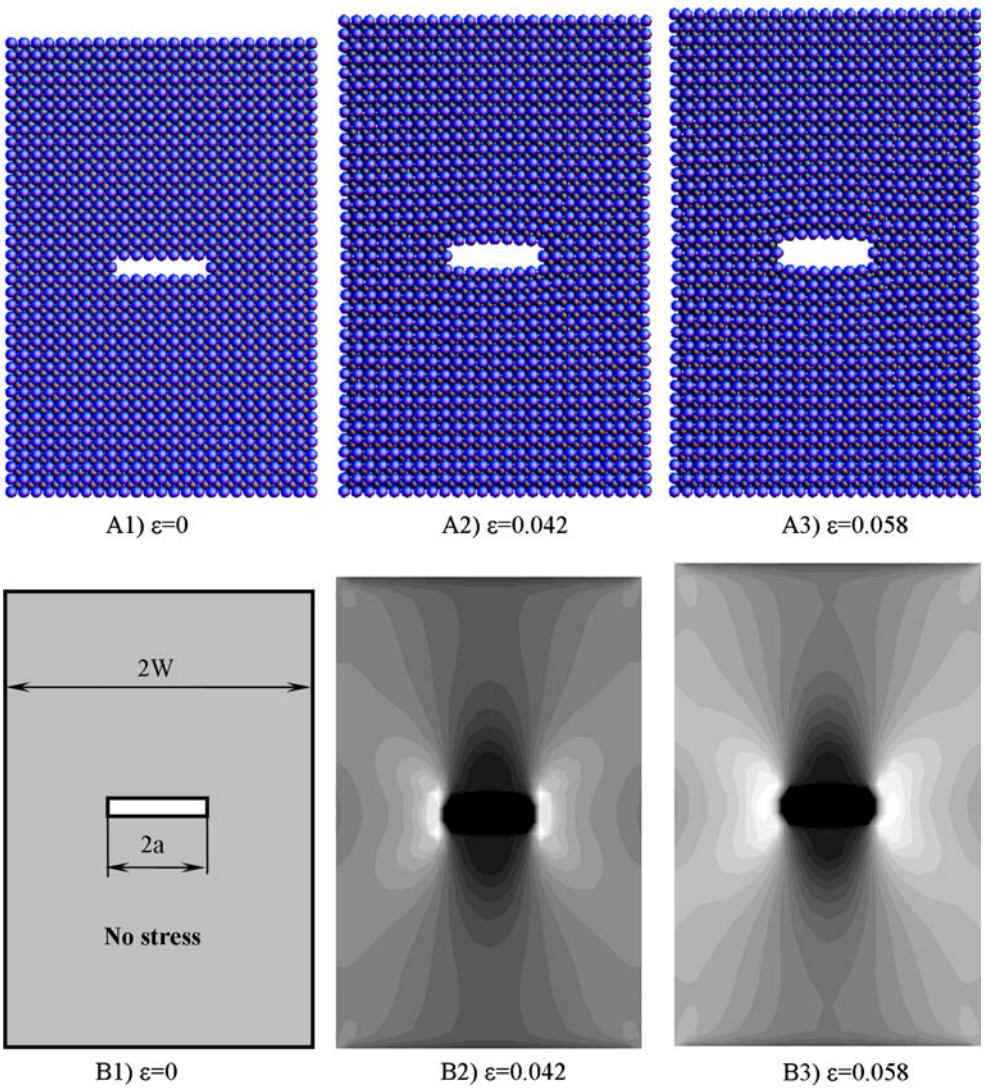

Fig. 9 Stages of sample degradation

Fig. 9 (continued)

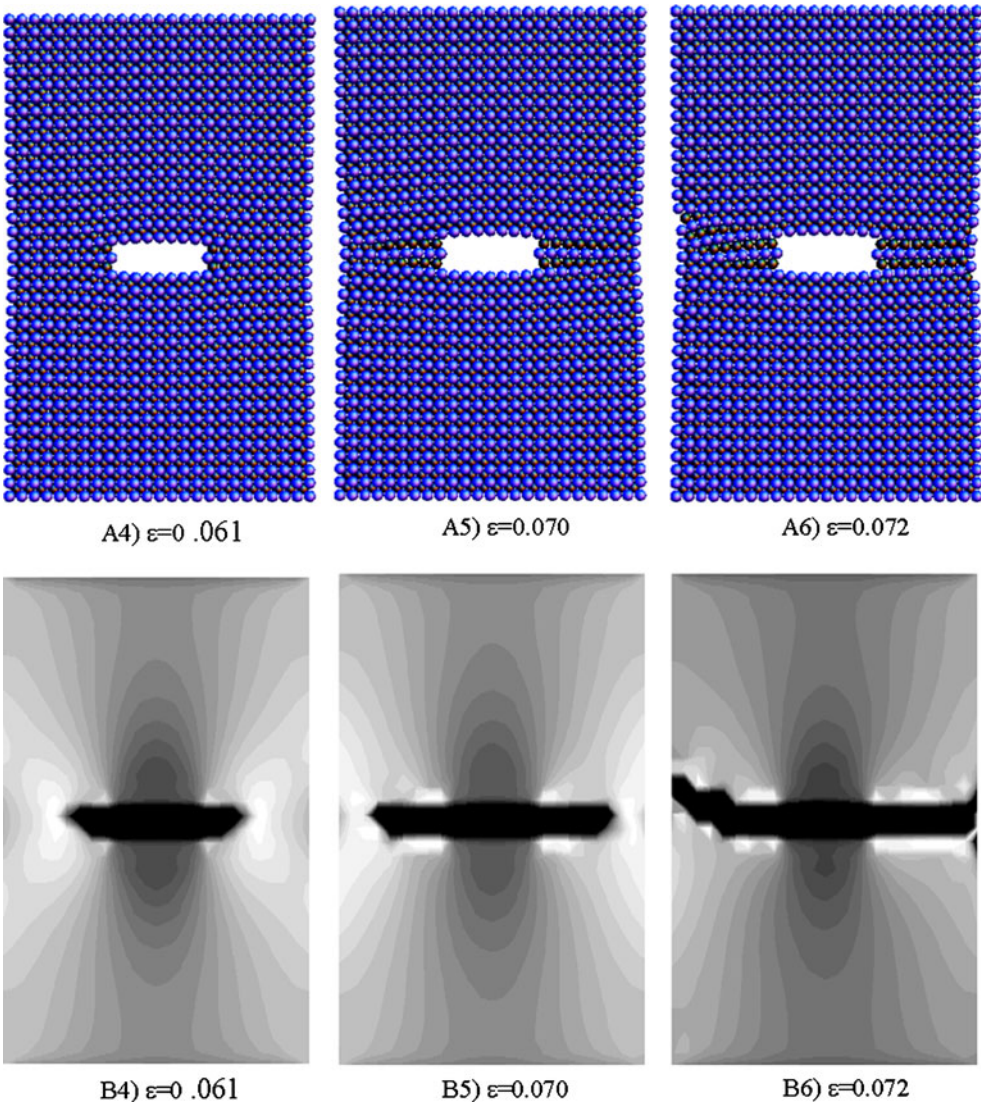

Figure 9(B5, B6) shows a "white" region of a high force concentration moving together with the expansion of the "black" zone of weakened bonds.

We find that demonstrating the interatomic force distribution at the edge of the crack is the most practical way to show defect configurations. Also, it allows the future growth paths of cracks or dislocations to be visualized. We hypothesized that a black/white border defines a new actual position for the tips of a growing crack; it is rather difficult to fix these based only on the analysis of atomic configuration (Fig. 9, A1–A5) while the proposed method allows the current location of the crack tips to be found quite easily from the direct observation of the force field contour plot (Fig. 9, B1–B5). The new crack length includes zones of weakened bonds, which, in a physical sense, are analogous to Barenblatt's cohesion zones.

In the vicinity of the left free boundary, an expansion of the weakened zone deviates from the original crack plane, simplifying the atomic plane sliding and creating a weak path for the crack to follow. Simultaneously, the right side of the crack keeps propagating in the same direction. At $\varepsilon = 0.072$, both left and right zones of weakened bonds reach the samples free boundaries, causing a significant stress drop in the stress-strain curve (Fig. 9, A6, B6; Fig. 10).

As the zones of weakened bonds spread across the entire uncracked ligament, the failure process can be considered as a general yield. At this point, the failure mode can switch from cleavage to sliding processes along the inclined slip lines (Fig. 9, B6; left side). These processes distort the arrangement of the atoms located between the crack tip and the cell's left boundary.

Further tensile loading leads to the sequence of events associated with sliding of atoms along the slip line, and results in final material degradation. This process is demonstrated in Fig. 9(A7, A8, A9), the core region being enlarged and the slip line shown in red in Fig. 9(A9).

Fig. 9 (continued)

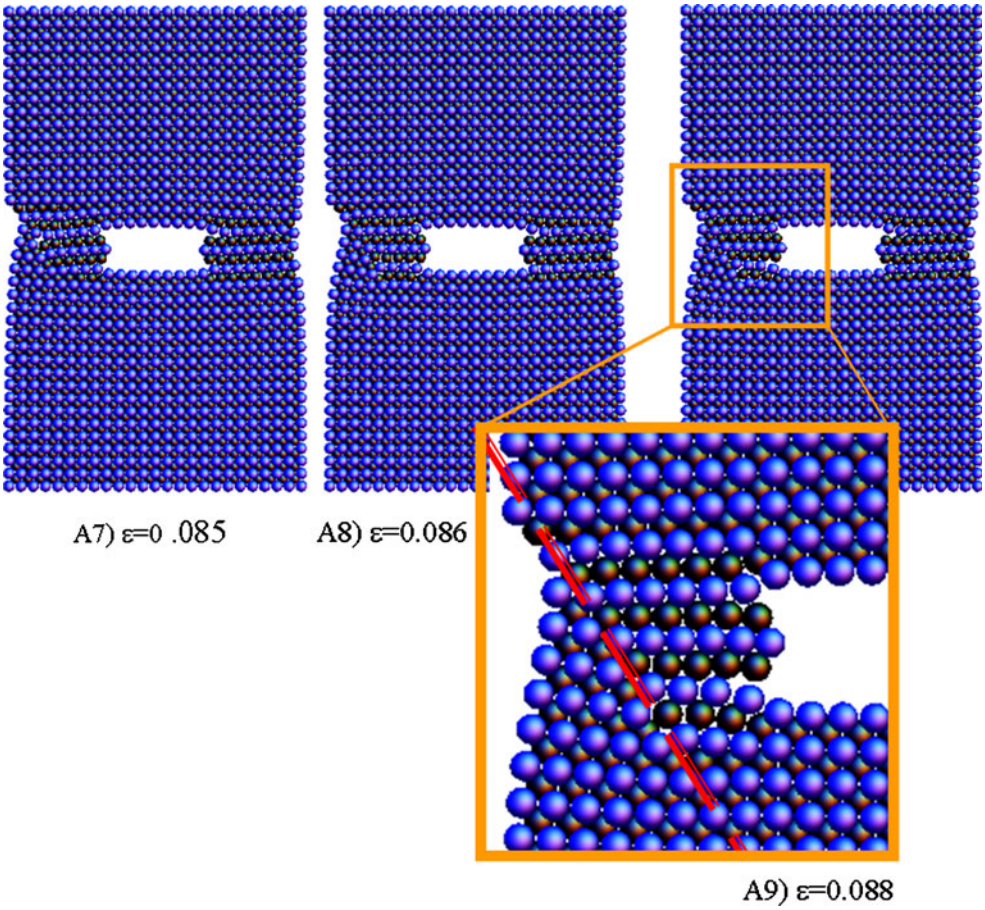

Summary

In the present paper we have demonstrated that IBA provides a practical tool for modeling of crack growth in iron crystals. The topology of the crystal structure was described by the structure stiffness matrix and its inverse. The stress–strain curve was obtained in a numerical tensile test. Each equilibrium state of the structure was found using the iterative procedure based on the IBA. The important feature of the applied relaxation technique is that it deals with updating the inverse of the stiffness matrix rather than with the stiffness matrix itself. Simulation allowed the strain and load at every element of atomic structure to be calculated. We found that the interatomic force distribution at the edge of the crack allowed the future growth paths of cracks or dislocations to be visualized. The results presented demonstrate the success of applying the IBA technique to modeling of large 2D and 3D systems of atoms interacting through strongly non-linear potential functions.

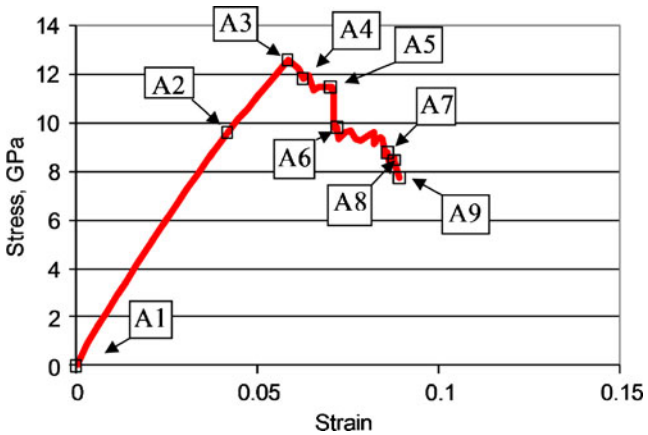

Fig. 10 Stress-strain curve

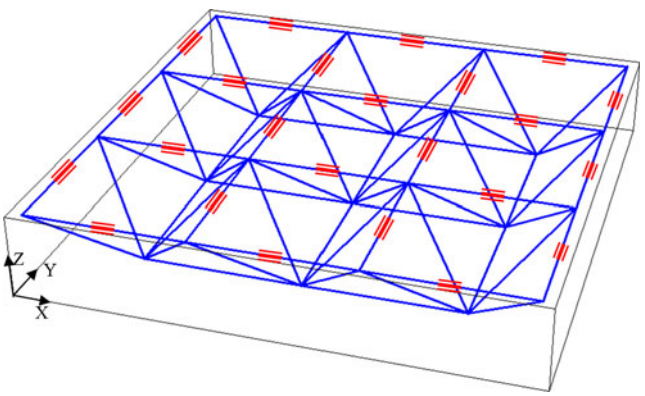

Fig. 11 Location of virtual strain gauges within the (001) plane

References

1. Telitchev IY, Vinogradov O (2008) J Mol Model 14:621–630
2. Hu SY, Ludwig M, Kizler P, Schmauder S (1998) Model Simul Mater Sci Eng 6:567–586
3. Kohlhoff S, Gumbsch P, Fischmeister HF (1991) Philos Mag A 4:851–878
4. Saraev D, Kizler P, Schmauder S (1999) Simul Mater Sci Eng 7:1013–1023
5. Shastry V, Farkas D (1996) Model Simul Mater Sci Eng 4:473–492
6. Farkas D, Hyde B (2005) Nano Lett 5:2403–240
7. Vinogradov O (2006) Int J Comput Methods 3:153–161
8. Press WH et al (1992) Numerical recipes: the art of scientific computing. Cambridge University Press, Cambridge
9. Martínez JM (2000) J Comput Appl Math 124:97–121
10. Cook RD, Plesha ME (1989) Concepts and applications of finite element analysis. Wiley, New York
11. Fujiwara T, Ishii Y (1980) J Phys F Met Phys 10:1901–1911
12. Girilfalco LA, Weizer VG (1959) Phys Rev 114:687–690
13. Lawn BR, Wilshaw TR (1975) Fracture of brittle solids. Cambridge University Press, Cambridge
14. Cheung KS, Yip S (1994) Model Simul Mater Sci Eng 2:865–892
15. Murakami Y (1987) Stress intensity factor handbook, vol 1. Pergamon, Oxford
16. Clatterbuck DM, Chrzan DC, Morris JW Jr (2002) Philos Mag Lett 82:141–147